University of Bath

Alternative formats
If you require this document in an alternative format, please contact:
openaccess@bath.ac.uk

Effects of ply angle and blocking on open-hole tensile strength of composite laminates: a design and certification perspective

T.R.C. Chuaqui[*a], M.W.D. Nielsen[a], J. Colton[b], R. Butler[a], A.T. Rhead[a]

[a] Materials and Structures Centre, Department of Mechanical Engineering, University of Bath, BA2 7AY Bath, UK

[b] School of Mechanical Engineering, Georgia Institute of Technology, GA 30332-0405 Atlanta, USA

Abstract

The failure strength of carbon-fibre reinforced plastic laminates under open-hole tension varies considerably with ply angle, ply blocking and loading direction. Here, laminates with various standard-angle and non-standard angle stacking sequences are subjected to both on- and off-axis loading in a comprehensive experimental and progressive damage finite element analysis testing campaign. It is found that interlaminar and intralaminar matrix damage can be beneficial when accumulated sub-critically in ply blocks aligned with loading direction, but can also lead to significant strength decreases owing to edge failure. In such cases, a numerical edge treatment is proposed for more accurate representation of open-hole tensile strength in large structures where holes are positioned away from free edges. The solution suppresses edge failure and results in up to 80% strength increases, challenging the validity of standard open-hole tension testing and current design rules for some applications.

Keywords: A. Carbon fibre, B. Strength, B. Stress concentrations, C. Finite element analysis (FEA).

1. Introduction

Establishing reliable and accurate allowables for notched strength of multidirectional carbon-fibre reinforced plastic (CFRP) laminates has become a pivotal step in the design and certification process of large aerospace components. To achieve this, extensive coupon testing is carried out under different loading conditions and considering different geometries. The particular case of open-hole tension (OHT) has received considerable attention, both because it is a simple and inexpensive test to perform, and because it is an early indicator of structural strength, representing the interaction of a common geometrical feature with fibre and matrix properties. OHT strength and underlying failure modes can change significantly with characteristics of the specimen; these have been extensively studied in recent years considering variations in laminate and ply block thickness, in-plane specimen scaling, changes in specimen width to hole diameter ratio and variations in ply percentage and stacking sequence [1–6]. A summary of these effects can be found in [5], where, ultimately, the accumulation of sub-critical interlaminar and intralaminar matrix damage and its

interaction with fibre failure were found to be the unifying factors that dictate OHT strength. It was found that sub-critical damage is mostly affected by ply blocking and can either increase specimen strength by blunting the notch in fibre dominated failure modes, or decrease it where failure is delamination-driven. The beneficial effects of sub-critical inter-fibre splitting of the main load bearing plies was also observed under multiaxial loading in [7, 8] for different stress raisers, using a modified Arcan test rig. It was verified that the degree of sub-critical damage varies with loading direction and lay-up. Recently, in [9], the progression of damage on the surfaces and inner plies of quasi-isotropic laminates under open-hole tension was recorded using *in-situ* edge microscopy and digital image correlation (DIC), providing *in-situ* evidence that variations in lay-up can lead to vastly different phenomena.

However, these studies have been conducted for the particular case of standard-angle (SA) laminates, comprised of the traditional 0°, ±45° and 90° ply orientations, and considering on-axis loading in the 0° ply direction only. OHT failure and the effects of ply blocking in less conventional laminates employing non-standard angle (NSA) with non-orthogonal ply orientations are still largely unexplored. NSA laminates have the potential to decrease manufacturing time, reduce stacking errors and facilitate laminate design selection, in particular in the form of dispersed stacking sequences using double set of double helix $[\pm \Phi / \pm \Psi]$ (double-double) angles [10–12]. In addition, NSA laminates can offer benefits in formability due to increased compatibility in ply deformation modes, decreasing the likelihood of manufaturing-induced defects [11, 13], and therefore, investigation of their performance is of interest. In [14] the effects of ply thickness and relative fibre angles were investigated for open-hole quasi-isotropic laminates under multiaxial loading, but these effects were analysed independently with only one dispersed NSA case being tested.

Moreover, the effects of ply blocking on OHT failure are often analysed from a scaling perspective, where either the ply block thickness in a laminate is increased, i.e ply-level scaling, or the number of repeating sublaminates is increased, i.e sublaminate-level scaling [1, 3–6]. These approaches provide insight into the fundamental physical mechanisms and key differences that drive ultimate failure, but do not necessarily provide a pathway to laminate tailoring for OHT strength considering other design requirements.

In this work, the effects of ply blocking and sub-critical damage are analysed from a design-based approach, considering comparable SA and NSA laminates and following, where possible, established aerospace design rules [15]. As such, the stacking sequence of SA and NSA laminates was varied from most dispersed to most blocked, keeping identical laminate thickness and in-plane stiffness, and preserving zero extension-shear and in-out-of-plane coupling terms. ±45° plies are positioned at the outer surfaces of SA laminates and a minimum of 10% thickness in each of the ply angles is used, for both SA and NSA cases.

A progressive damage meso-scale finite element (FE) model was implemented and experimen-

tally validated, both quantitatively (strength predictions) and qualitatively (failure mechanisms) using *post-mortem* ultrasonic C-scans. Validation of the model lays the basis for numerical analysis of a more extensive set of stacking sequences, providing insight into the exact location, sequence and interaction of different intralaminar and interlaminar damage events that lead to ultimate failure. The model presented in this work uses continuum damage mechanics (CDM) for the intralaminar damage modes and cohesive zones for the interlaminar regions. Within the CDM framework, mesh alignment with the fibre direction is used for each ply, preventing unrealistic crack paths and incorrect redistribution of local stresses typically associated with the inherent mesh dependency of CDM approaches. At the same time, this preserves simplicity, ease of implementation and relatively low computational cost when compared to discrete damage mechanics (DDM) approaches, such as the extended finite element method (XFEM).

The isolated and combined effects of ply blocking and off-axis loading of these laminates is investigated in detail using the model. For some cases, OHT strength is found to be largely misrepresented using the current standard method due to significant edge effects that cause fibre failure away from the hole. The validity and usefulness of the test for representation of OHT strength in large structural components, where holes are positioned away from free edges, is brought into question and a numerical solution based on a previously devised edge treatment [16, 17] is proposed within the FE framework to overcome testing limitations. The numerical edge treatment is a simple implementation that can be added to any progressive damage FE model, consisting of two narrow blocks of purely elastic CFRP material that are attached to each free edge of the specimens to prevent edge-driven failure. Finally, the use of unconventional laminates in aerospace applications, either employing NSA or considerable ply blocking, is briefly discussed in the light of this edge treatment.

2. Test methodology

Coupons with 100 mm gauge length, 36 mm width and 6 mm diameter holes at their centre point, were manufactured from AS4/8552 unidirectional prepreg and tested under displacement control in an Instron 5585H tensile test system using a pair of self-tightening tensile grips to determine OHT strength according to ASTM D5766-5766M [18], at a displacement rate of 0.5 mm/min. See Figure 1 for coupon dimensions and gripping regions, Table 1 for an overview of the coupons stacking sequences and Table 2 for the material properties of AS4/8552.

The stacking sequence of SA and NSA laminates was varied from most dispersed (SA1 and NSA1 cases) to most blocked (SA6 and NSA5 cases) with an applied on-axis displacement in the 0° direction, as shown in Figure 1. To approximate the cases of +5° and +10° off-axis loading, rotations by +5° and +10° were then applied to the stacking sequences of all coupons. Note that the original laminates without applied rotation are denoted as unmodified throughout the text.

Each unmodified laminate had 20 plies and their percentages were kept constant for both SA

cases with 50/40/10 for 0°, ±45° and 90° plies, respectively; and NSA cases with 60/40 for ±10° and ±57° plies, respectively. The in-plane stiffness **A** of all unmodified laminates is identical, with extension-shear terms $A_{16} = A_{26} = 0$ and in-out-of-plane coupling terms $\mathbf{B} \approx \mathbf{0}$. Stiffness matching of SA and NSA laminates follows the approach in [13].

The average strain through the specimens was extracted from DIC analysis, neglecting the peaks in strain around the hole and edges by averaging the data over a 200 mm² region, centred approximately 25 mm above the centre of the hole. Images were recorded at a frequency of 1 Hz until peak load using a pair of cameras in stereo, and then processed using DaVis software. The strain was extracted for one sample per laminate configuration only. The DIC strain data was smoothed using a 9th order polynomial, so that both linear or quasi-linear responses as well as non-linear regions are adequately captured. Finally, the experimental stress-strain curves were generated by merging the Instron load data with the DIC averaged strain data.

3. FE modelling framework

A three-dimensional meso-scale FE model was implemented using ABAQUS Explicit [19] in order to describe the mechanical behaviour of CFRP laminates. The modelling framework presented in this work is comprised of the following: (i) a combination of physically-based constitutive models that account for the ply and interlaminar behaviour, using surface-based cohesive zones to connect adjacent plies; (ii) two separate thermal and mechanical analysis steps to simulate the cool-down process after stress-free curing cycle and the loading of the specimens at ambient temperature; (iii) general contact in all model interior and exterior surfaces to prevent element interpentatration after intralaminar and interlaminar failure; (iv) appropriate kinematic considerations such as mesh alignment, directional biasing and element deletion to allow a physically-sound representation of the failure mechanisms.

The ply constitutive model is based on the models proposed by Tan et. al [20, 21], by Falco et. al [22] and by Maimí et. al [23, 24]. The best features of each model were selected in order to form the model presented in this work. As such, for more details on the fundamentals behind each modelling component, the reader is referred to the original articles. The models in [22–24] propose a coupled linear-exponential softening law for longitudinal tensile damage, accounting for both fibre breakage and pull-out but do not account for mixed-mode matrix damage progression, defining independent damage variables for the normal and shear stresses σ_{22} and τ_{12}. Therefore, to overcome this limitation, the matrix damage model presented in [20, 21] is used, which proposes a single matrix damage variable directly applied to the tractions acting on the fracture plane. In addition, the pre-damage shear response is modified with a Ramberg-Osgood model [25, 26] incorporating isotropic hardening, in order to account for non-linear elasto-plastic behaviour. Lastly, mesh alignment and element deletion criteria were implemented, following [22].

The influence of thermal residual stresses resulting from curing cool-down are accounted for

considering constant thermal expansion coefficients α_1, α_2 and half of the temperature drop (from $180°C$ for AS4/8552 to $25°C$). Consideration of the total temperature interval overestimates the residual stresses due to other attenuating parameters, such as humidity and moisture ingression, and therefore half of this value is used as per [22, 27].

Mechanical loading is subsequently applied by means of a smooth step velocity profile in the x-direction on one end-surface of the specimen, whilst enforcing zero velocity to fix the degrees-of-freedom of the other end-surface. For the smooth step profile, a sigmoid function increasing from 0 at instant $t = 0$ s to 2.5 mm/s at $t = t^f$ is used, where t^f corresponds to the final instant of the simulation. The value of t^f is calculated by integrating the sigmoid function and solving the displacement equation with respect to t, given a user-defined final displacement of 1 mm. Note that this value is not necessarily reached as simulations are automatically halted after a 40% drop in load from the maximum is detected. In order to guarantee a quasi-static solution, the energy ratio between kinetic and internal energy is monitored in every simulation, remaining below 5% in all cases. Owing to an in-plane deformation dominated response and to reduce computation time to a manageable level, one C3D8R linear element with reduced integration, enhanced hourglass and distortion control is used per ply thickness. A similar approach is used in [4, 22, 28]. A nominal density of $1.58 \cdot 10^{-6}$ kg/mm^3 [22] and a mass scaling ratio of 1000 were used to speed up the computation runtime without sacrificing the quasi-static nature of the simulation.

Mesh alignment with the orthotropic material directions has been shown to mitigate physically inadmissible crack propagation, which deviates from the microstructure-allowed path due to mesh induced stress locking [29]. Incorrect crack bands not only lead to an unrealistic representation of the failure mechanisms, but can also result in inaccurate ultimate strength predictions. The strategy used in [22] is adopted, where the imposition of physically-sound crack paths as a result of mesh alignment is reinforced by directional biasing using an element aspect ratio of 1 to 3 (transverse to longitudinal directions). A mesh generator was implemented in Python, creating fibre aligned partitions in each ply, for any given coupon geometry. These are then introduced in the ABAQUS model, where each partition is seeded with the selected element sizing, generating the final mesh for each ply. A schematic of the model is shown in Figure 2. The material properties used in the model are shown in Table 2.

3.1. Ply behaviour

The ply behaviour is described by a continuum damage model, implemented in a material user subroutine (VUMAT), and accounts for three main independent failure mechanisms: matrix failure under a general three-dimensional stress state, longitudinal tensile failure and longitudinal compressive failure.

Prior to damage initiation, the material response is linear elastic in longitudinal and transverse directions, and non-linear elasto-plastic in shear, such that plastic strains ε_{ij}^p only exist for $i \neq j$. The pre-damage non-linear shear behaviour is predicted with a uni-dimensional Ramberg-Osgood

model [25, 26] in each shear component:

$$\sigma_{ij} = \frac{2G_{ij}\varepsilon_{ij}}{\left(1 + \left(\frac{G_{ij}2\varepsilon_{ij}}{\tau_A}\right)^n\right)^{\frac{1}{n}}}, \; ij = 12, 23, 13 \tag{1}$$

where G_{ij} are the elastic shear moduli and τ_A and n are the Ramberg-Osgood parameters, found by fitting the experimental shear stress-strain curves of the material [30]. Permanent plastic deformation is accounted for using rate-independent isotropic hardening. A more detailed description of the fundamentals of isotropic hardening and its implementation can be found in [31, 32].

Each failure process begins with the onset of irreversible damage, defined by three-dimensional failure criteria established in [33]. The criteria for matrix and longitudinal compressive failure are evaluated considering the stress tensor acting on oblique fracture planes $\wp$ and ψ, respectively. For the matrix failure fracture plane $\wp$, only a single rotation of the stress tensor is needed (see Figure 3a), whereas for longitudinal compressive failure, three successive rotations of the stress tensor are required: from material coordinate system to the kinking plane θ, to the misalignment frame φ and finally to the fracture plane ψ (see Figure 3b). The determination of $\wp$ and ψ requires the maximisation of the corresponding criteria between $\wp, \psi \in [\,0, \pi\,[$. To reduce the number of necessary iterations in the maximisation problem, a golden section search algorithm combined with inverse parabolic interpolation was used [34]. Angles θ and φ can be calculated according to [33], where a numerical solution using Newton-Raphson's method considering linear elastic behaviour is applied. This approach is here extended to account for non-linear shear described by Ramberg-Osgood equation.

Besides the elastic constants, the failure criteria require X_T, X_C, Y_T, Y_C and S_L, corresponding to the longitudinal tensile, longitudinal compressive, transverse tensile, transverse compressive and shear ply strengths, respectively. The criteria also require prior determination of ply *in-situ* strengths and friction coefficients, which can be calculated according to [35–37]. After the criteria are met, energy-based damage evolution laws are applied so that the stresses acting on the fracture plane that define a crack surface can be degraded. Complete failure occurs when the material no longer carries load, i.e the stresses acting on the fracture plane in a given failure mode are null.

For both tensile and compressive longitudinal failure, damage is applied on fracture planes orthogonal to the fibre orientation by the damage variable $d_F \in [0, 1]$. Tensile and compressive longitudinal damage are accounted for independently by tracking two distinct variables d_F^+ and d_F^-. Under longitudinal tension, the evolution of d_F^+ follows a coupled linear-exponential law, as shown in Figure 4a. The initial linear softening phase is dictated by fibre breakage, where energy $f_G \mathcal{G}_1^+ / l_F$ is dissipated. The exponential portion corresponds to fibre pull-out, dissipating energy $(1 - f_G) \mathcal{G}_1^+ / l_F$. The total dissipated energy corresponds to the critical strain energy release rate of the material for longitudinal tension $\mathcal{G}_1^+$ normalised by the longitudinal characteristic finite element length l_F. Under longitudinal compression, the evolution of d_F^- follows a linear softening

response, as shown in Figure 4b, corresponding to the propagation of a kink band and dissipating the normalised critical strain energy release rate for longitudinal compression $\mathcal{G}_1^-/l_F$. After complete energy dissipation, the material preserves a fraction of its load bearing capacity as a plateau is reached, corresponding to kink band broadening at constant stress. To ensure closure of longitudinal cracks under load reversal, the total longitudinal damage variable d_F is expressed as:

$$d_F = d_F^+ \frac{\langle \tilde{\sigma}_{11} \rangle}{|\tilde{\sigma}_{11}|} + d_F^- \frac{\langle -\tilde{\sigma}_{11} \rangle}{|\tilde{\sigma}_{11}|} \tag{2}$$

A more detailed description of the implementation of linear and coupled linear-exponential softening laws for longitudinal failure can be found in [23, 24].

For matrix failure, damage is applied on the oblique fracture plane $\wp$ using the damage variable $d_M \in [0,1]$. Linear softening material response is considered, dissipating the critical mixed-mode energy release rate, normalised by the characteristic finite element length l_M. The mode-mixity ratio is established by a quadratic relationship considering the stress state at onset of damage on the fracture plane $\wp$ and the mode I and II ply critical strain energy release rates, $\mathcal{G}_2^+$ and $\mathcal{G}_6$, according to [20]. The corresponding uni-axial shear and transverse material responses can be observed in Figures 4c and 4d, respectively.

The true, damaged stress tensor $\boldsymbol{\sigma}^\wp$ can be expressed as a function of the effective stress tensor $\tilde{\boldsymbol{\sigma}}^\wp$ and the damage tensor $\mathbf{D}$ considering strain equivalence on the fracture plane $\wp$, which in turn can be written as a function of the rotation tensor $\mathbf{R}^\wp$, the orthotropic elasticity tensor $\mathbf{C^0}$ and the elastic strain tensor $\boldsymbol{\varepsilon}^e$:

$$\boldsymbol{\sigma}^\wp = \mathbf{D}\tilde{\boldsymbol{\sigma}}^\wp = \mathbf{D}\mathbf{R}^\wp \mathbf{C^0} \boldsymbol{\varepsilon}^e \tag{3a}$$

$$\mathbf{D} = \operatorname{diag}\left\{ 1-d_F, \ 1 - \frac{\langle \tilde{\sigma}_{22}^\wp \rangle}{\tilde{\sigma}_{22}^\wp} d_M, \ 1, \ 1-d_M, \ 1-d_M, \ 1 \right\} \tag{3b}$$

where $\boldsymbol{\varepsilon}^e$ can be determined from the plastic and total strain tensors $\boldsymbol{\varepsilon}^e = \boldsymbol{\varepsilon} - \boldsymbol{\varepsilon}^p$. Note that d_M is not applied when the effective normal stress on the fracture plane $\tilde{\sigma}_{22}^\wp < 0$, as this would effectively close the crack. In order to maintain a positive definite elasticity tensor, the Poisson's ratios must also be degraded after damage initiation. This is achieved by directly degrading each component ν_{ij} in $\mathbf{C^0}$ using global damage variables d_{ii}, with $i = 1, 2, 3$ according to [20].

The irreversibility of damage is accounted for both d_F, d_M and d_{ii} with $i = 1, 2, 3$ such that, given an instant t and increment in time Δt:

$$d_k^{t+\Delta t} = \max\left\{ 0, \min\left\{ 1, \max\left\{ d_k^t, d_k^{t+\Delta t} \right\} \right\} \right\}, k = F, M, 11, 22, 33 \tag{4}$$

Element deletion is enforced when the criteria suggested in [22] are met in order to avoid highly distorted elements and to model crack opening [21].

The characteristic finite element lengths can be determined by computing $l_i = V_{el}/A_i$, $i = F, M$,

7

where V_{el} corresponds to the element volume and A_i corresponds to the area of the polygon resulting from the intersection of the fracture plane with the element. Mesh alignment with fibre orientation greatly simplifies the computation of A_F and A_M. Moreover, the maximum element sizing was determined *a priori* according to [38], ensuring that the fracture energy is larger than the elastic energy per unit surface area, preventing a snap-back in the material response.

3.2. Interlaminar behaviour

A general mixed-mode cohesive model was implemented to capture delaminations using in-built surface-based frictionless cohesive behaviour in ABAQUS Explicit [19]. The damage onset is predicted by means of a quadratic stress criterion [39]. Uncoupled penalty stiffnesses $K = 10^6$ N/mm^3 are used in the initial linear elastic cohesive response to avoid contributing to the global compliance of the specimens. The values were determined after conducting a sensitivity analysis, and provide an accurate and stable material response whilst maintaining a reasonable computational runtime. After damage initiation, the tractions on the interface are linearly decreased to zero, dissipating the critical mixed-mode strain energy release rate, obtained by the Benzeggagh-Kenane (BK) criterion [40] using a BK parameter $\eta_{BK} = 1.45$ [22]. The ply nominal strengths Y_T, S_L and mode I and II critical strain energy release rates $\mathcal{G}_2^+$, $\mathcal{G}_6$, respectively, were used at the interfaces. Standard double cantilever (DCB) and end-notch flexural (ENF) simulations were performed and compared with analytical solutions using linear elastic fracture mechanics (LEFM) to confirm the validity of the interlaminar model.

3.3. Numerical edge treatment

The numerical edge treatment follows the approach in [16, 17], where narrow resin blocks are attached to the free edges of 4-point and 3-point bending specimens, successfully mitigating free edge interlaminar stresses and delaying edge failure. It was observed, however, that edge failure could never be completely suppressed due to material discontinuity in the CFRP-resin block interface. Using a block material with the same elastic behaviour as the CFRP whilst preventing fracture is not possible experimentally, but can be easily achieved in a virtual framework. As such, the numerical edge treatment in this work consists of two 1 mm wide blocks with purely elastic behaviour and no stiffness degradation in either interlaminar or intralaminar regions in order to prevent fracture. The blocks are attached to each free edge of the specimen using tie constraints on the connecting surfaces, as shown in Figure 2. Continuity of elastic constants from the CFRP to the treatment blocks is ensured by using the same stacking sequence in the blocks as in the specimens, eliminating stress concentrations at the CFRP-block transition. Moreover, the element width sizing used in the blocks is similar to the CFRP specimen in order to preserve a smooth transition of the stress field.

4. Results

The quantitative and qualitative agreement between the FE model and experimentally tested laminates is shown in Figures 5, 6 and 7, respectively.

Figure 5a shows the comparison between OHT failure strength predicted by the model and corresponding experimental mean (and standard deviation). Two sets of results are shown, the first, displayed in light grey, corresponding to the National Center for Advanced Materials Performance (NCAMP) experimental campaign performed in [22], where three OHT laminate configurations are tested using AS4/8552 pre-preg: a soft laminate (SO) with stacking sequence [45/-45/0/45/-45/90/45/-45/45/-45]$_S$; a quasi-isotropic laminate (QI) with [-45/0/45/90]$_{2S}$; and a hard laminate (HA) with [0/45/0/90/0/-45/0/45/0/-45]$_S$. The second set, in dark grey, corresponds to the laminates tested in-house. Note that the specimen dimensions of the first set are slightly different (6.35 mm and 38.1 mm diameter and width, respectively) and these results are used for model validation purposes only. In the second set, standard deviations are not shown in cases where a single experiment was performed, with three repeats being performed otherwise.

In Figure 5b, the Bland-Altman plot [41] of the OHT strengths from Figure 5a is shown, demonstrating the agreement of the model with the experiments on a general level. The difference between experimental (S_{Exp}) and FEA (S_{FEA}) solutions are plotted against their mean for the total 32 in-house experiments, plus 3 experiments from [22]. The mean of the differences, the standard deviation ($\pm$SD) and the limits of agreement between the experiments and the FE model at $\pm$1.96SD are also shown.

Figure 6 shows the comparison between the experimental and FE predicted stress-strain curves until ultimate strength. Note, however, that one experimental stress-strain curve is shown per laminate configuration as DIC was performed for a single sample only. Therefore, the experimental ultimate strengths highlighted in the Figure 6 correspond to a single point rather than the experimental mean presented in Figure 5a.

Figure 7 shows the comparison of C-scanned and FE predicted post-failure morphology of the coupons. The depth of the delaminated areas shown by C-scans is indicated by a colour map and outer surface cracks are represented in greyscale. The FEA images are displayed in translucent greyscale. Note that C-scans are post-test and thus show more extensive damage, whereas FE simulations are halted after a 40% drop in load. Relative propensity for damage and its morphology are, however, comparable. The results presented hereafter were all obtained from the FE model.

Figure 8 shows the FE strength predictions of all laminates in Table 1, except +5° rotated laminates. Four sets of results can be observed for both SA and NSA laminates: unmodified laminates, laminates with numerical edge treatment (+E), laminates with rotation (+10°) and laminates with rotation and numerical edge treatment (+10°+E).

Figure 9 shows the effects of ply blocking on the onset of intralaminar matrix damage ($d_M > 0$) and fibre damage ($d_F > 0$) in unmodified SA and NSA laminates, plotted against strain at ultimate

failure. The onset of matrix and fibre failure are shown for each ply orientation of each laminate.

Figures 10 and 11 show the effects of ply blocking on the accumulation of intralaminar matrix damage in unmodified SA and NSA laminates. In Figure 10 a quantitative analysis is performed by computing the ratio of damaged elements ($d_M > 0$) over the total number of elements, until ultimate failure. Figure 11 shows the qualitative effects of ply blocking on intralaminar matrix cracking, and three representative examples (SA1, SA3 and SA6) for SA and (NSA1, NSA3 and NSA5) for NSA laminates are shown at ultimate failure. Matrix cracks in plies with identical orientation are highlighted in the same colour: in SA laminates, red, green and blue correspond to $\pm 45°$, $0°$ and $90°$ plies, respectively and in NSA laminates, red and blue correspond to $\pm 57°$ and $\pm 10°$ plies, respectively. Note that matrix cracks correspond to the particular case of fully damaged material due to matrix tensile failure.

Figures 12 and 13 show the effects of ply blocking on the severity of delaminations in SA (SA2 case is omitted as it is very similar to SA1) and NSA laminates, respectively. The first, second and third rows of Figures 12 and 13 correspond to unmodified laminates, laminates rotated by $10°$ and laminates rotated by $10°$ with numerical edge treatment, respectively. Laminates with only numerical edge treatment and no rotation (+E) were not shown for brevity, as they were not as affected by delaminations as the rotated cases. Contour lines of fully delaminated areas are plotted for every interface, with different colours corresponding to different interfaces. For the sake of clarity, the depth of each interface is not provided. In unmodified and rotated cases (first and second rows), the delamination contours were obtained at an applied strain ε_{xx}^0 corresponding to ultimate failure. In the rotated with numerical edge treatment cases (third row), the delamination contours were obtained at an applied strain equivalent to the strain at ultimate failure of the corresponding rotated laminates (second row), to allow a direct comparison.

Figures 14 and 15 show the effects of the applied rotation on intralaminar damage mechanisms of a blocked SA laminate, using the comparison of SA5 and SA5+$10°$ as an illustrative case. In Figure 14, a top view of the laminates at three applied strains (before, at and after ultimate failure) are shown. Matrix cracks of different plies are shown in different colours and propagation of fibre damage ($d_F > 0$) is represented in a colour map (see Figure caption for more details). The rotation leads to a change in failure type: from hole-driven to edge-driven failure. The causes and implications of this are addressed in detail in the discussion section. Figure 15 shows the cross-section of Figures 14a, 14b, 14d and 14e, taken at 9 mm away from the centre of the hole in the x direction (this location is indicated on each aforementioned Figure). Differences in concentration and unloading of longitudinal stress (σ_{11}) for hole-driven and edge-driven failure are shown in a colour map on the cross-section plane, whereas delaminations and matrix cracks are displayed in translucent greyscale.

Finally, in Figure 16 the complete stress-strain curves obtained from FEA are shown for both SA and NSA cases, from smallest to largest amount of ply blocking, with +$10°$ and without rotations,

with (+E) and without edge treatment.

5. Discussion

5.1. Model validation

Figure 5a indicates that the FE model is able to accurately capture failure strength of coupons with various stacking sequences, with a maximum relative difference of approximately 5% from the experimental mean. In particular, as this correlation lays the basis for numerical analysis of additional stacking sequences and the failure mechanisms at play in each, it is noted that model is able to correctly predict the failure strength of coupons with: (i) off-axis angles (e.g. NSA1-3 and laminates with rotated stacking sequences); (ii) imbalance of plies about the loading axis (e.g. laminates with rotated stacking sequences); (iii) blocked and dispersed sequences (e.g. SA3 vs SA1); (iv) and combinations of each of these e.g. (SA3+10°). In addition, from Figure 5b, the systematic error of the model is found to be negligible, with a 2.6 MPa mean of differences between experiments and corresponding FE predictions. No proportional error is found either, as the variation of these differences is independent of the magnitude of laminate strength. Lastly, the standard deviation (SD) of the differences between experiments and FE predictions is also small, corresponding to 26.9 MPa, resulting in very good limits of agreement at ±1.96 SD from the mean. This indicates that significant changes in behaviour predicted by the FE model, associated to very large strength variations (typically > 100 MPa), e.g SA2 to SA3 or SA4/SA5 to SA6 in Figure 8a, or conversely, invariance in strength of the NSA cases in Figure 8b, depict real physical effects.

Figure 6 suggests that good agreement is also found between the experimental and the FE predicted stress-strain curves. Small discrepancies fall within material variability and experimental inaccuracies.

Comparison of images in Figure 7 shows that the FE model is also able to qualitatively predict fracture patterns, not only displaying similar intralaminar failure but also comparable relative propensity for delamination, e.g. blocked sequences show a greater extent of interlaminar damage in both C-scans and FEA. With the capability of the FE model now established, the remaining discussion uses FEA only to explore the effects of stacking sequence and misalignment of load on OHT strength.

5.2. The effects of ply blocking on OHT failure of SA and NSA laminates

In this section, the effects of ply blocking are initially analysed considering unmodified laminates only (SA1-SA6 and NSA1-NSA5). Figure 8 shows comparatively blocked SA stacking sequences (e.g SA3) outperform NSA laminates. However, NSA laminates are very insensitive to ply blocking, with variation in stacking sequence leading to only marginal changes in OHT strength, when compared to SA laminates.

11

The effects of ply blocking on ultimate failure crucially depend on the ability or inability of a laminate to accumulate sub-critical damage. As a result, in SA laminates ply blocking has a pronounced effect on OHT strength by significantly affecting the accumulation of sub-critical interlaminar and intralaminar matrix damage. Conversely, the invariability in OHT strength to different NSA stacking sequences stems from the inability of these laminates to accumulate sub-critical damage whilst retaining load-bearing capacity.

5.2.1. Sub-critical damage in SA and NSA laminates

In SA laminates, intralaminar matrix damage initiates in ±45° and/or 90° plies and is followed by intralaminar matrix damage in 0° plies, as shown in Figure 9. Fibre damage is the last failure mechanism and can initiate in 0° and/or ±45° plies depending on stacking sequence. Loss of load-bearing capacity in these plies generally dictates ultimate failure in SA laminates. In particular, 0° plies fail due to fibre breakage only, and intralaminar matrix damage can accumulate independently without compromising their load-bearing capacity. In ±45° plies, intralaminar damage mechanisms cannot accumulate independently, but ultimately, fibre failure is dominant in SA laminates. Therefore, delaying the onset of fibre damage corresponds to increased OHT strength in SA laminates, as shown in Figure 9.

In NSA laminates, intralaminar matrix damage initiates in the softer ±57° plies, followed by the stiffer ±10° plies, as shown in Figure 9. Onset of fibre failure occurs after and only in the ±10° plies but does not necessarily correlate with ultimate failure. The effect of fibre failure on ultimate OHT strength is less critical in NSA laminates, as the load-bearing capacity is shared between fibre and matrix (with the contribution of each depending on ply orientation) in every ply. Unlike SA laminates, intralaminar matrix damage in NSA laminates cannot accumulate sub-critically in any given ply without affecting the rest of the laminate and without inevitably leading to complete failure.

5.2.2. Effects of ply blocking on sub-critical interlaminar and intralaminar matrix damage

Increased block thickness facilitates the propagation of intralaminar matrix damage after its onset within that block of plies. This results in an increased rate of accumulated damage in laminates where accumulation of sub-critical damage is possible. This is demonstrated in Figure 10a, where the order of SA laminates with ascending ratio of damaged elements, for a given applied strain, coincides with the blocking order SA1 to SA6. This is also shown in the examples in Figures 11a, 11b and 11c, where intralaminar matrix cracking visibly increases in ply blocking order. In addition, ply blocking leads to greater stress discontinuities at interfaces, due to increased stress gradients through block thickness, which promote earlier onset of interlaminar damage. It also reduces the number of interfaces, with more energy being available per block interface to propagate those delaminations. These effects can be observed in the case of SA laminates in Figure 12, where increased ply blocking clearly leads to more extensive delaminations.

In SA laminates, blocking 0° plies can result in an increase in OHT strength, as the additional intralaminar matrix damage and delaminations in adjacent block interfaces blunt the notch and reduce local fibre stress concentrations, effectively delaying the onset of fibre failure. This corresponds to cases SA1 to SA2, SA2 to SA3 and SA5 to SA6, as shown in Figure 8a, where the maximum 0° block thickness increases from 1 to 2, 2 to 4 and 5 to 10 plies, respectively. This blunting effect has been discussed in detail in [1, 3–6].

Blocking of 90° plies has practically no consequence on OHT strength, as shown from SA3 to SA4 in Figure 8a. This is because the onset of overall fibre damage, in Figure 9, is virtually unaffected by either increase in intralaminar matrix damage of the 90° block or by adjacent block interface delaminations. Note that from SA3 to SA4 the maximum 0° block thickness is also increased from 4 to 5 plies, but this is not sufficient to yield a visibile effect.

Blocking ±45° plies, results in a decrease in OHT strength as the increased accumulation of interlaminar and intralaminar matrix damage leads to an earlier onset of fibre failure. This is shown from SA4 to SA5 in Figure 9. In this case, these mechanisms directly affect fibre damage in blocks of ±45° plies, but unlike NSA laminates, they are far less critical and can accumulate as 0° plies provide the necessary stiffness.

In NSA laminates, accumulation of significant sub-critical damage is not possible and therefore, ply blocking yields very little effect on the extent of intralaminar matrix damage, as shown quantitatively in Figure 10b and qualitatively in Figures 11d, 11e, 11f. Interlaminar damage is also marginally affected by ply blocking in NSA laminates, as shown in Figure 13. Comparatively, NSA laminates display less extensive delaminations than SA counterparts due to ply non-orthogonality, which results in an increased compatibility in elastic constants of adjacent blocks of plies. As a consequence, blocks of plies can deform more freely, leading to less pronounced interlaminar stresses near the hole and free edges at block interfaces, and reducing the effect of blocking on these stresses. Ultimately, this decreases the extent of delaminations and its variability with ply blocking.

The effects of ply blocking are also illustrated in Figure 16, where the increase in interlaminar and intralaminar matrix damage result in more pronounced non-linear behaviour, particularly in SA cases with significant ply blocking, such as SA6 in Figure 16f. Conversely, the reduced extent of these damage mechanisms in NSA cases results in a response that remains closer to linear behaviour, even in blocked cases such as NSA5 in Figure 16k.

5.3. Validity of OHT testing: Shortcomings and proposed numerical edge treatment

5.3.1. Edge-driven fibre failure

Rotating the laminates by +10° to mimic off-axis loading resulted in significant differences in interlaminar damage, as shown in Figures 12 and 13. From comparison of the unmodified cases with their +10° rotated version, it was observed that the applied rotation led to increased delamination severity in both SA+10° and NSA+10° laminates, which becomes more pronounced

in SA+10° cases with ply blocking. Delamination morphology also changed after rotation and is similar in all laminates, with triangular shaped areas at the free edges. These two observations can be attributed to the introduction of extension-shear coupling due to the applied +10° rotation. The additional in-plane shearing, combined with the test boundary conditions, leads to an increase in both interlaminar and intralaminar shear stresses, especially near the free edges, which promote delaminations and intralaminar matrix damage.

The increase in delaminations and intralaminar matrix damage near the free edges can lead to a change in fibre failure type, from hole-driven to edge-driven. This type of failure occurs when delaminations and matrix cracks growing from the free edges are severe enough to generate stress concentrations which load the fibres past their ultimate strength, leading to fibre rupture, which propagates near the free edges. This does not necessarily mean that fibre damage exclusively develops at the free edges and not at the hole, but rather that these two occur concurrently and eventually coalesce. The change from hole-driven to edge-driven fibre failure is illustrated in Figure 14, where SA5 displays fibre damage propagating from the hole towards the free edges, whereas SA5+10° displays fibre damage occurring concurrently at the hole and near the free edges, where considerable matrix cracking induces significant fibre stresses. This can be observed in Figure 15, where longitudinal stress σ_{11} concentrates in the vicinity of matrix cracks near the free edge of SA5+10°, leading to fibre damage and subsequent unloading of σ_{11} in 10° plies from those cracks towards the hole. This contrasts with hole-driven failure, as shown in the SA5 case, where σ_{11} unloads evenly from the hole towards the free edges.

The combination of ply blocking, ply orthogonality and extension-shear coupling promote edge-driven fibre failure in SA3+10° to SA6+10° cases in Figure 8a. This type of failure leads to a significant reduction in OHT strength when compared to the corresponding unmodified laminates. In the remaining SA+10° and NSA+10° cases in Figures 8a and 8b, the relative decrease in OHT strength, when compared to the corresponding unmodified versions, is much smaller, as the increase in interlaminar and intralaminar matrix damage due to the applied rotation is not sufficient to trigger edge-driven failure. The NSA laminates analysed are particularly insensitive to edge-driven failure, even in cases with significant ply blocking and applied rotations. This is because of reduced interlaminar damage due to ply non-orthogonality and inability to accumulate intralaminar matrix damage, both of which remain under the threshold that triggers edge-driven failure.

5.3.2. Effects of numerical edge treatment

The standard OHT test method [18] specifies that specimens with non-acceptable failure modes, i.e failure that does not occur at the hole, should be rejected as they are not representative of OHT strength in large parts. However, as demonstrated by the cases simulated in this work, it can be impossible to identify edge-driven failure via visual inspection of failed specimens as ply cracking always occurred at the hole, regardless of failure type. However, prevention of edge-driven failure is possible in a simulation environment by virtually removing the free edges using the previously

described numerical edge treatment. The effects of the numerical edge treatment on OHT strength can be observed by comparing laminates with $+E$ label with the corresponding versions without $+E$ in Figure 8. Edge-driven failure is suppressed in SA3+10°+E to SA6+10°+E, resulting in significant increases in strength (up to 80%) when compared to corresponding cases SA3+10° to SA6+10°. The numerical edge treatment also had an effect on the SA6+E OHT strength, suggesting that failure of SA6 is negatively affected by free edge effects. Qualitatively, it can be observed from Figures 12 and 13 that the numerical edge treatment successfully supresses free edge delaminations in every case, whilst preserving similar delamination contours around the hole. The effects on OHT strength, however, are confined to laminates where failure is partially or completely edge-driven. In cases where failure is already hole-driven, the numerical edge treatment leads to a very small increase in strength due to the additional stiffness provided by the purely elastic block material, as shown in the remaining cases in Figure 8. This indicates that the procedure can be used to reliably predict large part OHT strength without interference from edge-driven failure.

5.4. Challenging design rules: Unconventional stacking sequences and ply orientations

The possibility of predicting the real OHT strength of large parts, where holes are positioned away from free edges, using the numerical edge treatment in a simulation framework opens up opportunities in laminate design. Limiting maximum laminate block thickness to approximately 0.5 mm or less is a common aerospace design guideline [15] and would normally exclude some unconventional blocked SA laminates, such as SA6. This practice would be supported if the standard test method were followed, as a small misalignment in load would trigger unrealistic edge-driven failure resulting in a significant reduction in strength. However, results with numerical edge treatment in Figure 8a indicate that such blocked laminates would be excellent choices for larger parts with holes away from the free edges.

Alternatively, the NSA laminates in this study, either with ply blocking or off-axis loading, are unaffected by edge-driven failure and display very little variation in strength, which is on par with dispersed SA strength. Such properties make them well suited to OHT strength prediction with current test procedures and makes for a robust and reliable design process.

6. Conclusions

A comprehensive physically-based FE model was developed for open-hole tension (OHT), implemented in ABAQUS and successfully validated against experimental tests on laminates featuring standard and non-standard angles, imbalance of plies about the loading axis, and blocked and dispersed stacking sequences. A maximum relative difference of 5% was observed in predicted and experimental strength, with a very small mean of differences between experimental observations and FEA (2.6 MPa). Very good agreement is also found between FE predicted failure morphology and *post-mortem* C-scans. The FE model provided insight into the failure processes that drive differences in ultimate OHT failure strength.

SA laminates with blocked 0° plies were found to have higher OHT strengths than both NSA and dispersed SA laminates with identical in-plane stiffness, under on-axis 0° loading. This is due to increased sub-critical interlaminar and intralaminar matrix damage in thick 0° blocks and adjacent interfaces, which blunt fibre stresses delaying ultimate failure. However, blocked SA laminates performed poorly under off-axis loading (here mimicked by laminate rotation), displaying much lower OHT strength than both dispersed SA and NSA counterparts under similar loading conditions. This is due to edge-driven fibre failure which is promoted by the combination of extension-shear coupling, ply orthogonality and significant ply blocking, which cause critical interlaminar and intralaminar matrix damage at the free edges.

A numerical edge treatment that supresses edge-driven fibre failure, in order to mimic boundaries found in large composite parts, was found to produce significant increases in strength. In particular, blocked SA laminates, which would be ruled out by current OHT testing procedures as offering low off-axis strength, actually display up to 80% higher strength when using this edge treatment, bringing into question the usefulness of standard OHT coupon testing when holes are positioned away from free edges.

On the other hand, OHT strength of NSA laminates studied here was much less sensitive to either variations in ply blocking or on/off-axis loading, and was not affected by edge-driven fibre failure. These observations can be attributed to: intralaminar matrix damage cannot accumulate sub-critically and leads to ultimate failure; non-orthogonality between plies produces less extensive and less variable interlaminar damage. Such laminates can be reliably tested using current testing standards and provide OHT strengths on par with dispersed SA stacking sequences. However, as a general guideline, simulations with numerical edge treatment are recommended to accurately test any laminate where the type of OHT failure is not known in advance. This paves the way for more reliable virtual design and certification of large components, where holes are positioned away from free edges, using high-fidelity meso-scale OHT coupon modelling.

7. Acknowledgements

References

[1] B.G. Green, M.R. Wisnom, and S.R. Hallett. An experimental investigation into the tensile strength scaling of notched composites. *Composites Part A: Applied Science and Manufacturing*, 38:867–878, 2007.

[2] P.P. Camanho, P. Maimí, and C.G. Dávila. Prediction of size effects in notched laminates using continuum damage mechanics. *Composites Science and Technology*, 67:2715–2727, 2007.

[3] M.R. Wisnom and S.R. Hallett. The role of delamination in strength, failure mechanism and hole size effect in open hole tensile tests on quasi-isotropic laminates. *Composites Part A: Applied Science and Manufacturing*, 40:335–342, 2009.

[4] S.R. Hallett, B.G. Green, W.G. Jiang, and M.R. Wisnom. An experimental and numerical investigation into the damage mechanisms in notched composites. *Composites Part A: Applied Science and Manufacturing*, 40:613–624, 2009.

[5] S.R. Hallett, B.G. Green, W. Jiang, K.H. Cheung, and M.R. Wisnom. The open hole tensile test : a challenge for virtual testing of composites. *International Journal of Fracture*, 158:169–181, 2009.

[6] M.R. Wisnom, S.R. Hallett, and C. Soutis. Scaling Effects in Notched Composites. *Journal of Composite Materials*, 44(2):195–210, 2010.

[7] J.L.Y. Tan, V.S. Deshpande, and N.A. Fleck. Failure mechanisms of a notched CFRP laminate under multi-axial loading. *Composites Part A: Applied Science and Manufacturing*, 77:56–66, 2015.

[8] J.L.Y Tan, V.S. Deshpande, and N.A. Fleck. The effect of laminate lay-up on the multi-axial notched strength of CFRP panels: Simulation versus experiment. *European Journal of Mechanics / A Solids*, 66:309–321, 2017.

[9] F.E Oz, M. Mehdikhani, N. Ersoy, and S.V. Lomov. In-situ imaging of inter- and intra-laminar damage in open-hole tension tests of carbon fibre-reinforced composites. *Composite Structures*, 244(March):112302, 2020.

[10] S.W. Tsai, S. Sihn, J.D.D. Melo, A. Arteiro, and R. Rainsberger. Composite Laminates theory and practice of analysis, design and automated layup. In *Composite Laminates theory and practice of analysis, design and automated layup*, pages 113–185. Stanford Aeronautics & Astronautics, 2017.

[11] K.J. Johnson, R. Butler, E.G. Loukaides, C. Scarth, and A.T. Rhead. Stacking sequence selection for defect-free forming of uni-directional ply laminates. *Composites Science and Technology*, 171:34–43, 2019.

[12] S. Shrivastava, N. Sharma, S.W. Tsai, and P.M. Mohite. D and DD-drop layup optimization of aircraft wing panels under multi-load case design environment. *Composite Structures*, 248(May):112518, 2020.

[13] M.W.D. Nielsen, K.J. Johnson, A.T. Rhead, and R. Butler. Laminate design for optimised in-plane performance and ease of manufacture. *Composite Structures*, 177:119–128, 2017.

[14] T. Laux, K. Wui, J.M. Dulieu-Barton, and O.T. Thomsen. Ply thickness and fibre orientation effects in multidirectional composite laminates subjected to combined tension/compression and shear. *Composites Part A*, 133(March):105864, 2020.

[15] M.C.Y Niu. Airframe structural design - Practical design information and data on aircraft structures. In *Advanced Composite Structures*, pages 492–537. Hong Kong: Conmilit Press Limited, 2nd edition, 1999.

[16] T.A. Fletcher, T. Kim, T.J. Dodwell, R. Butler, R. Scheichl, and R. Newley. Resin treatment of free edges to aid certification of through thickness laminate strength. *Composite Structures*, 146:26–33, 2016.

[17] T.R.C. Chuaqui, E. Sebastian, V. Sahadevan, A.T. Rhead, and R. Butler. Edge treatment of short beam shear tests for improved assessment of structural strength. *Composites Part A: Applied Science and Manufacturing*, 137(105991), 2020.

[18] American Society for Testing and Materials. ASTM D5766/D5766M-11. Standard Test Method for Open-Hole Tensile Strength of Polymer Matrix Composite Laminates.

[19] ABAQUS Documentation. Dassault Systèmes Simulia Corp, Providence, RI.

[20] W. Tan, B.G. Falzon, L.N.S. Chiu, and M. Price. Predicting low velocity impact damage and Compression-After-Impact (CAI) behaviour of composite laminates. *Composites Part A: Applied Science and Manufacturing*, 71:212–226, 2015.

[21] W. Tan, B.G. Falzon, and M. Price. Predicting the crushing behaviour of composite material using high-fidelity finite element modelling. *International Journal of Crashworthiness*, 20(1):60–77, 2015.

[22] O. Falcó, R.L. Ávila, B. Tijs, and C.S. Lopes. Modelling and simulation methodology for unidirectional composite laminates in a Virtual Test Lab framework. *Composite Structures*, 190:137–159, 2018.

[23] P. Maimí, P.P. Camanho, J.A. Mayugo, and C.G. Dávila. A continuum damage model for composite laminates: Part I - Constitutive model. *Mechanics of Materials*, 39:897–908, 2007.

[24] P. Maimí, P.P. Camanho, J.A. Mayugo, and C.G. Dávila. A continuum damage model for composite laminates: Part II - Computational implementation and validation. *Mechanics of Materials*, 39:909–919, 2007.

[25] T.A. Bogetti, C.P.R. Hoppel, V.M. Harik, J.F. Newill, and B.P. Burns. Predicting the nonlinear response and progressive failure of composite laminates. *Composites Science and Technology*, 64:329–342, 2004.

[26] T.A. Bogetti, C.P.R. Hoppel, V.M. Harik, J.F. Newill, and B.P. Burns. Predicting the nonlinear response and failure of composite laminates: correlation with experimental results. *Composites Science and Technology*, 64:477–485, 2004.

[27] A. Puck and H. Schürmann. Failure analysis of FRP laminates by means of physically-based phenomenological models. *Composites Science and Technology*, 62:1633–1662, 2002.

[28] C. Furtado, G. Catalanotti, A. Arteiro, P.J. Gray, B.L. Wardle, and P.P. Camanho. Simulation of failure in laminated polymer composites: Building-block validation. *Composite Structures*, 226:111168, 2019.

[29] M. Jirásek and T. Zimmermann. Analysis of Rotating Crack Model. *Journal of Engineering Mechanics*, 124(8):842–851, 1998.

[30] K. Marlett. Hexcel 8552 AS4 Unidirectional Prepreg at 190 gsm & 35% RC Qualification Material Property Data Report. Technical report, National Institute for Aviation Research, Wichita, 2011.

[31] J.C. Simo and T.J.R. Hughes. *Computational inelasticity*. Springer, 1998.

[32] O. Cousigné, D. Moncayo, D. Coutellier, P. Camanho, H. Naceur, and S. Hampel. Development of a new nonlinear numerical material model for woven composite materials accounting for permanent deformation and damage. *Composite Structures*, 106:601–614, 2013.

[33] G. Catalanotti, P.P. Camanho, and A.T. Marques. Three-dimensional failure criteria for fiber-reinforced laminates. *Composite Structures*, 95:63–79, 2013.

[34] J. Wiegand, N. Petrinic, and B. Elliott. An algorithm for determination of the fracture angle for the three-dimensional Puck matrix failure criterion for UD composites. *Composites Science and Technology*, 68:2511–2517, 2008.

[35] P.P. Camanho, C.G. Dávila, S.T. Pinho, L. Iannucci, and P. Robinson. Prediction of in situ strengths and matrix cracking in composites under transverse tension and in-plane shear. *Composites Part A: Applied Science and Manufacturing*, 37:165–176, 2006.

[36] G. Catalanotti. Prediction of in situ strengths in composites: Some considerations. *Composite Structures*, 207:889–893, 2019.

[37] C.G. Dávila, P.P. Camanho, and C.A. Rose. Failure Criteria for FRP Laminates. *Journal of Composite Materials*, 39(4):323–345, 2005.

[38] Z.P. Bažant and B.H. Oh. Crack band theory for fracture of concrete. *Matériaux et Constructions*, 16(93):155–177, 1983.

[39] L. Ye. Role of Matrix Resin in Delamination Onset and Growth in Composite Laminates. *Composites Science and Technology*, 33:257–277, 1988.

[40] M.L. Benzeggagh and M. Kenane. Measurement of Mixed-Mode Delamination Fracture Toughness of Unidirectional Glass/Epoxy Composites With Mixed-Mode Bending Apparatus. *Composites Science and Technology*, 56:439–449, 1996.

[41] J.M. Bland and G.D Altman. Statistical methods for assessing agreement between two methods of clinical measurement. *The Lancet*, (February 8):307–310, 1986.
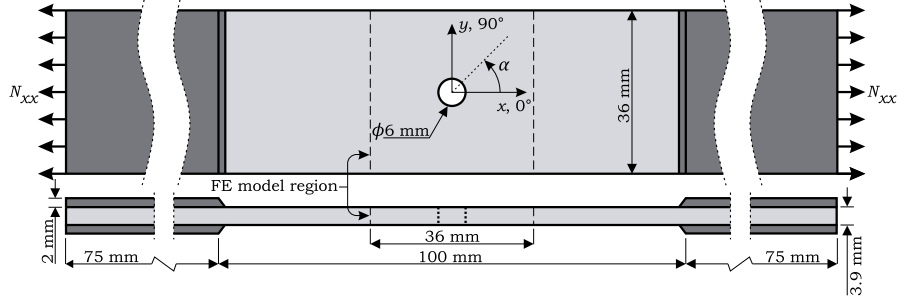
Figure 1: Schematic of OHT specimen showing dimensions, coordinate system, arbitrary ply orientation α and loading N_{xx}. Square region (36x36 mm) used in the FE model is also highlighted.
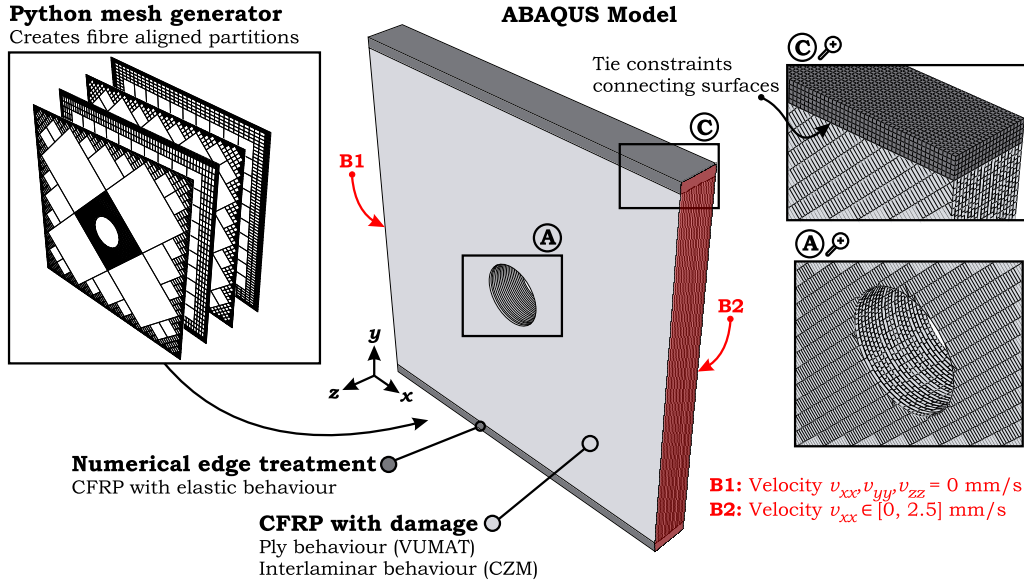

Figure 2: Schematic of OHT FE model, corresponding to the square region (36x36 mm^2) highlighted in Figure 1. Example shows the case of a coupon with numerical edge treatment. Cases without numerical edge treatment are identical but without the additional 1 mm wide elastic CFRP blocks. Boundary conditions B1 and B2 applied on left and right hand-side surfaces, corresponding to a 0 mm/s velocity and a 0 to 2.5 mm/s smooth step velocity profile, respectively.
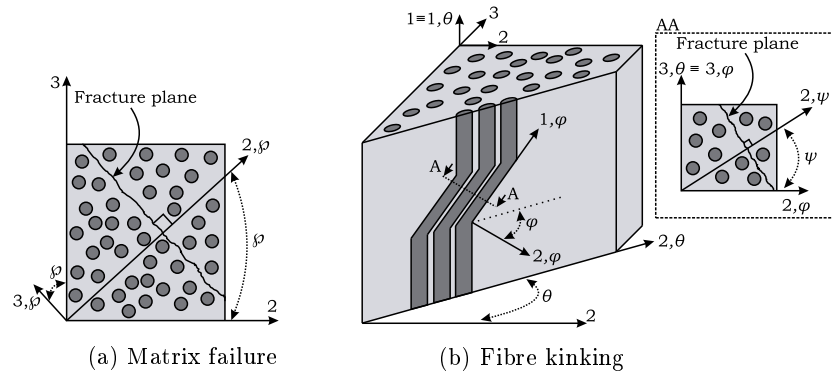

(a) Matrix failure

(b) Fibre kinking

Figure 3: Rotations of stress tensor onto fracture plane for matrix and londitudinal compressive (fibre kinking) failure criteria. In (a), rotation of the material coordinate system to the matrix fracture plane $\wp$ by angle $\wp$ about the fibre orientation 1-axis. In (b), three consecutive rotations of the material coordinate system to arrive at kinking fracture plane ψ: rotation θ about 1-axis; rotation φ about 3,θ-axis; rotation ψ about 1,φ-axis.

20

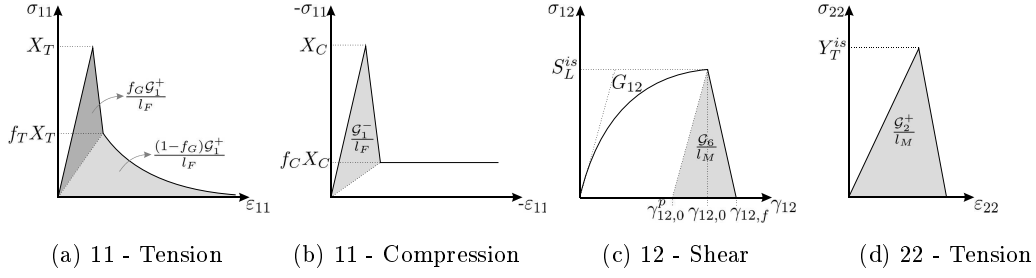(a) 11 - Tension (b) 11 - Compression (c) 12 - Shear (d) 22 - Tension

Figure 4: Uniaxial material response under longitudinal tension, longitudinal compression, in-plane shear (with $\gamma_{12} = 2\varepsilon_{12}$) and transverse tension considered in FE model. $\gamma_{12,0}^{p}$, $\gamma_{12,0}$, $\gamma_{12,f}$ correspond to plastic shear strain at onset of damage, total shear strain at onset of damage and final shear strain, respectively.

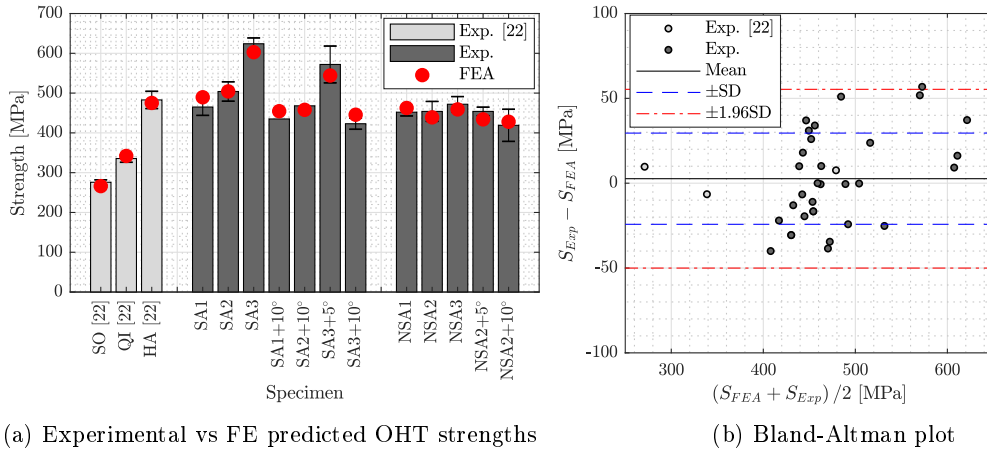(a) Experimental vs FE predicted OHT strengths

(b) Bland-Altman plot

Figure 5: In (a), comparison of experimental mean and FE predicted OHT strengths. Set of experiments in light grey from NCAMP experimental campaign from [22]. Set of experiments in dark grey performed in-house, where standard deviations are not shown in cases where a single experiment was performed or three repeats performed otherwise. In (b), Bland-Altman plot of the OHT strengths from FEA (S_{FEA}) and experiments (S_{Exp}) using all 32 in-house experimental datapoints (in dark grey), plus the 3 datapoints from [22] (in light grey). Mean of differences $S_{Exp} - S_{FEA}$, $\pm$ standard deviation ($\pm$SD) and $\pm$1.96 standard deviation of differences ($\pm$1.96SD) are also shown.
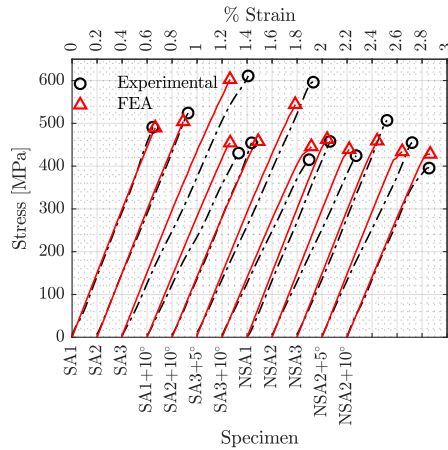

Figure 6: Comparison of experimental and FE predicted stress-strain curves until ultimate strength, with one experimental sample per laminate configuration. Different configurations are offset by 0.2% from each other to improve readability. FE curves were cropped post peak load for direct comparison with experimental curves and ultimate strength is highlighted with markers in all cases. For the complete FE curves, the reader is referred to Figure 16.
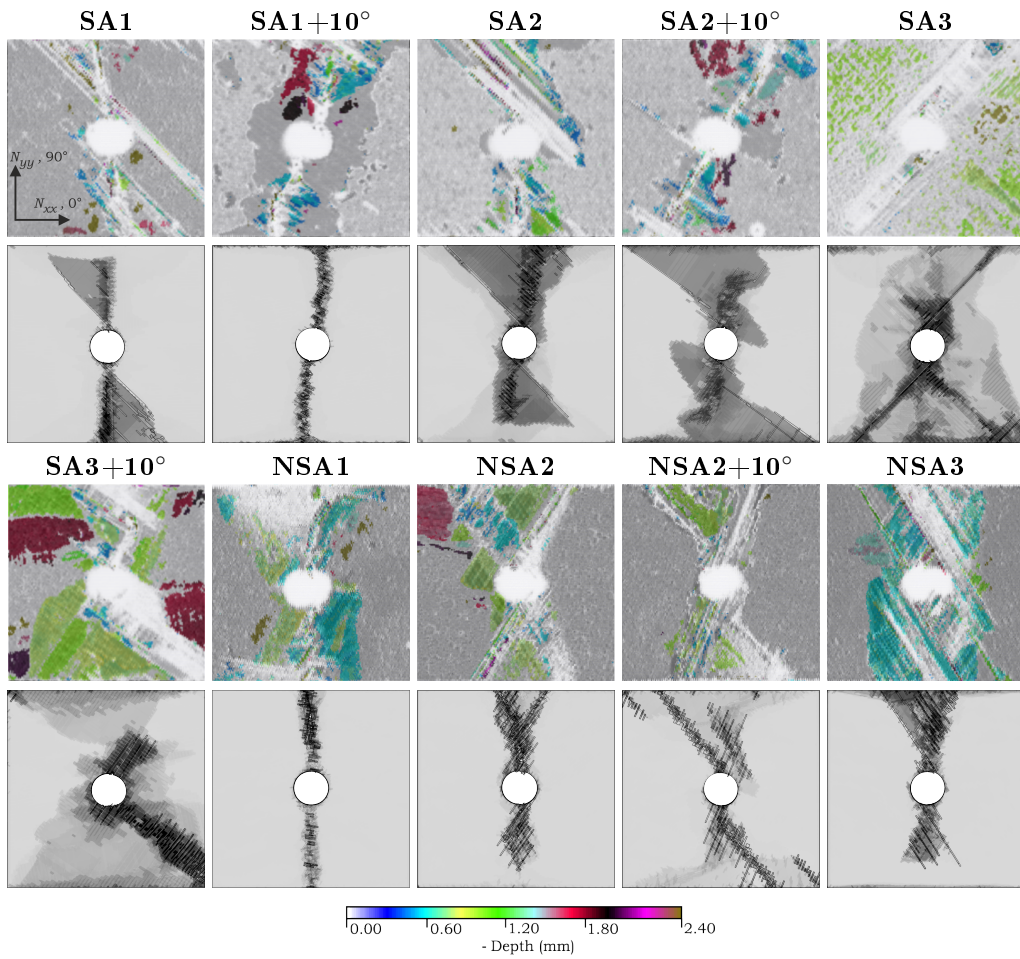
Figure 7: Comparison of C-scanned and FEA predicted *post-mortem* failure morphology of coupons. Depth of delaminated areas shown by overlaid time of flight ultrasonic C-scans is indicated by a colour map and outer surfaces are represented in greyscale. Delaminations and intralaminar cracking displayed in translucent greyscale in FEA. Loading direction in x.
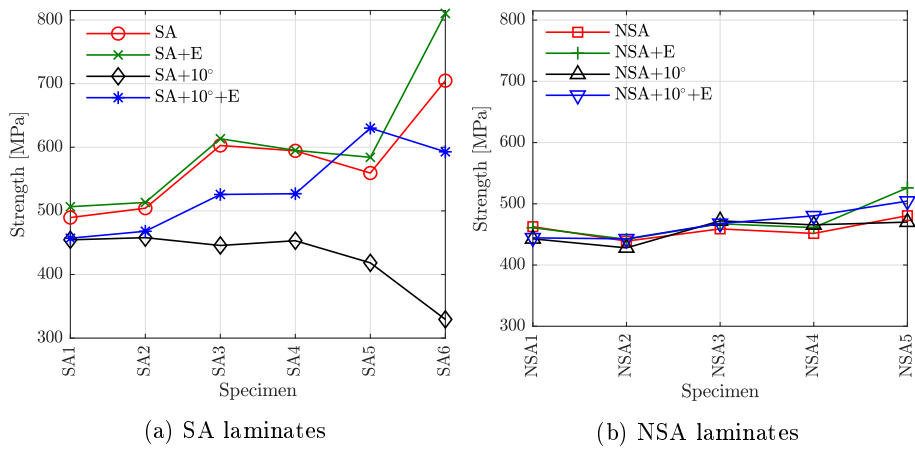

(a) SA laminates

(b) NSA laminates

Figure 8: OHT strength predictions of SA and NSA laminates using FEA, with ($+10°$) and without rotation and with ($+E$) and without numerical edge treatment. Stacking sequence is varied from most dispersed (SA1 and NSA1 cases) to most blocked (SA6 and NSA5 cases).
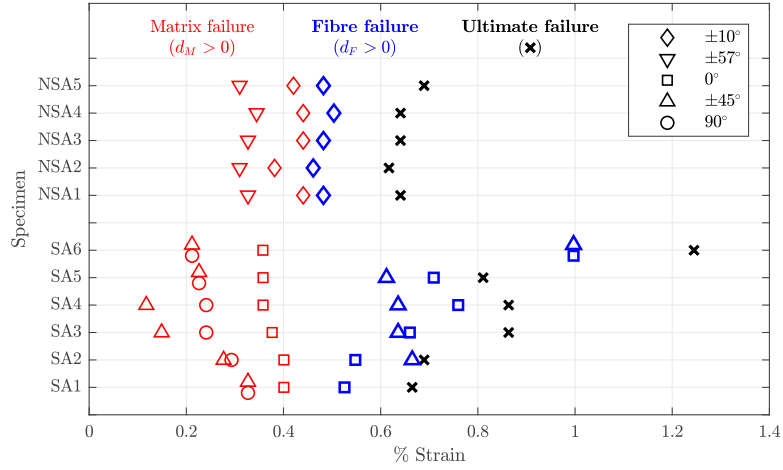
Figure 9: Onset of intralaminar failure mechanisms predicted by FEA (fibre damage - $d_F > 0$ and matrix damage - $d_M > 0$) in 0°, ±45° and 90° plies of unmodified SA laminates, and in ±10° and ±57° plies in unmodified NSA laminates. Ultimate failure is also plotted for each laminate. Stacking sequence is varied from most dispersed (SA1 and NSA1 cases) to most blocked (SA6 and NSA5 cases).

(a) SA laminates
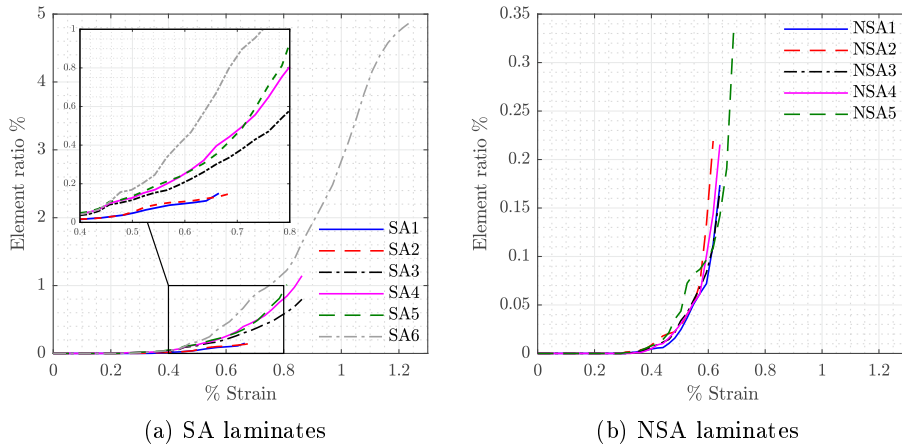
(b) NSA laminates

Figure 10: Effect of different ply blocking strategies on the accumulation of intralaminar matrix damage in laminates using FEA. The ratio of damaged elements (due to intralaminar matrix damage $d_M > 0$) over total number of elements in unmodified SA and NSA laminates is used as a metric for damage accumulation. Curves are plotted until strain at ultimate failure. Stacking sequence is varied from most dispersed (SA1 and NSA1 cases) to most blocked (SA6 and NSA5 cases).

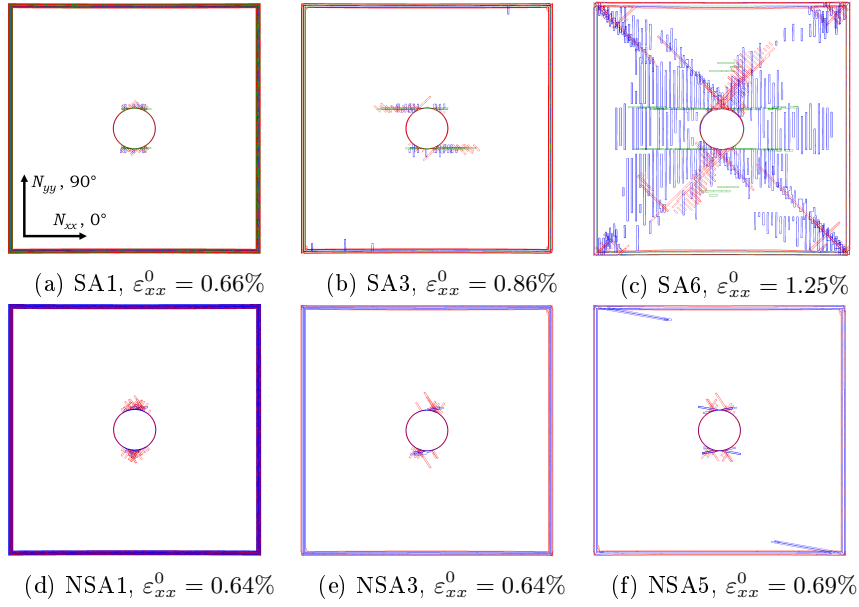(a) SA1, $\varepsilon_{xx}^0 = 0.66\%$ (b) SA3, $\varepsilon_{xx}^0 = 0.86\%$ (c) SA6, $\varepsilon_{xx}^0 = 1.25\%$

(d) NSA1, $\varepsilon_{xx}^0 = 0.64\%$ (e) NSA3, $\varepsilon_{xx}^0 = 0.64\%$ (f) NSA5, $\varepsilon_{xx}^0 = 0.69\%$

Figure 11: Effects of ply blocking on intralaminar matrix cracking predicted by FEA ($d_M \geq 0.999 \wedge \sigma_{22}^\wp \geq 0$) at ultimate failure for three representative cases, for both SA and NSA laminates. Red, green and blue correspond to $\pm 45°$, $0°$ and $90°$ plies, respectively, in SA laminates. Red and blue correspond to $\pm 57°$ and $\pm 10°$ plies, respectively, in NSA laminates. ε_{xx}^0 corresponds to applied strain at ultimate failure. Transparency added to the material to make matrix cracks visible in every plie. Loading direction in x.

Figure 12: Delamination contour plots of SA laminates for different ply blocking strategies from FEA. Second row with rotation ($+10°$) and third row with rotation and numerical edge treatment ($+10° + $ E). Different colours correspond to different ply interfaces. ε_{xx} corresponds to applied strain and ε_{xx}^0 corresponds to applied strain at ultimate failure. Transparency added to the material to make delaminations visible in every interface. Loading direction in x. Stacking sequence is varied from most dispersed (SA1 case) to most blocked (SA6 case).
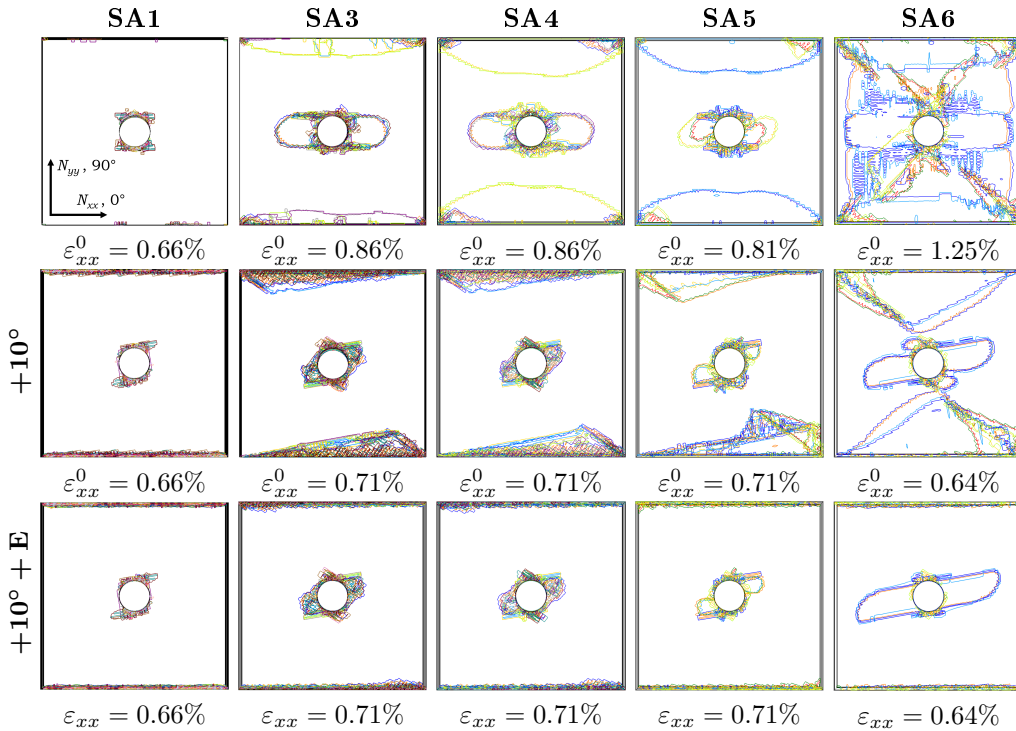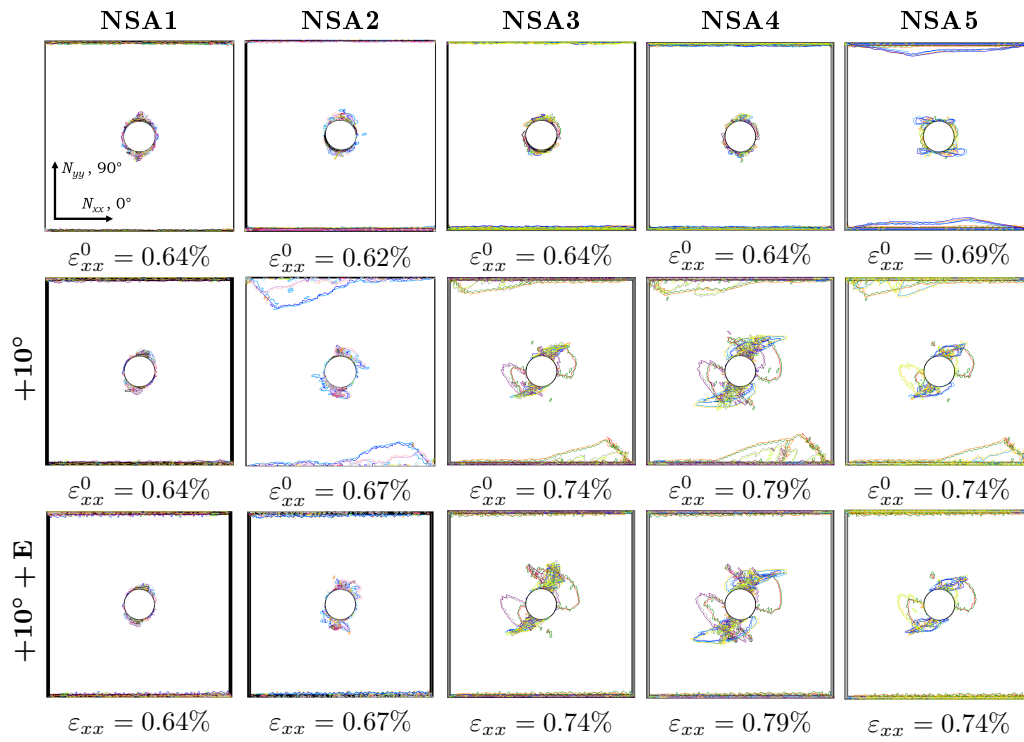
Figure 13: Delamination contour plots of NSA laminates for different ply blocking strategies from FEA. Second row with rotation ($+10°$) and third row with rotation and numerical edge treatment ($+10° + \mathrm{E}$). Different colours correspond to different ply interfaces. ε_{xx} corresponds to applied strain and ε_{xx}^0 corresponds to applied strain at ultimate failure. Transparency added to the material to make delaminations visible in every interface. Loading direction in x. Stacking sequence is varied from most dispersed (NSA1 case) to most blocked (NSA5 case).

(a) SA5, $\varepsilon_{xx} = 0.76\%$ (b) SA5, $\varepsilon_{xx}^0 = 0.81\%$ (c) SA5, $\varepsilon_{xx} = 0.86\%$

(d) SA5+10°, $\varepsilon_{xx} = 0.67\%$ (e) SA5+10°, $\varepsilon_{xx}^0 = 0.71\%$ (f) SA5+10°, $\varepsilon_{xx} = 0.76\%$
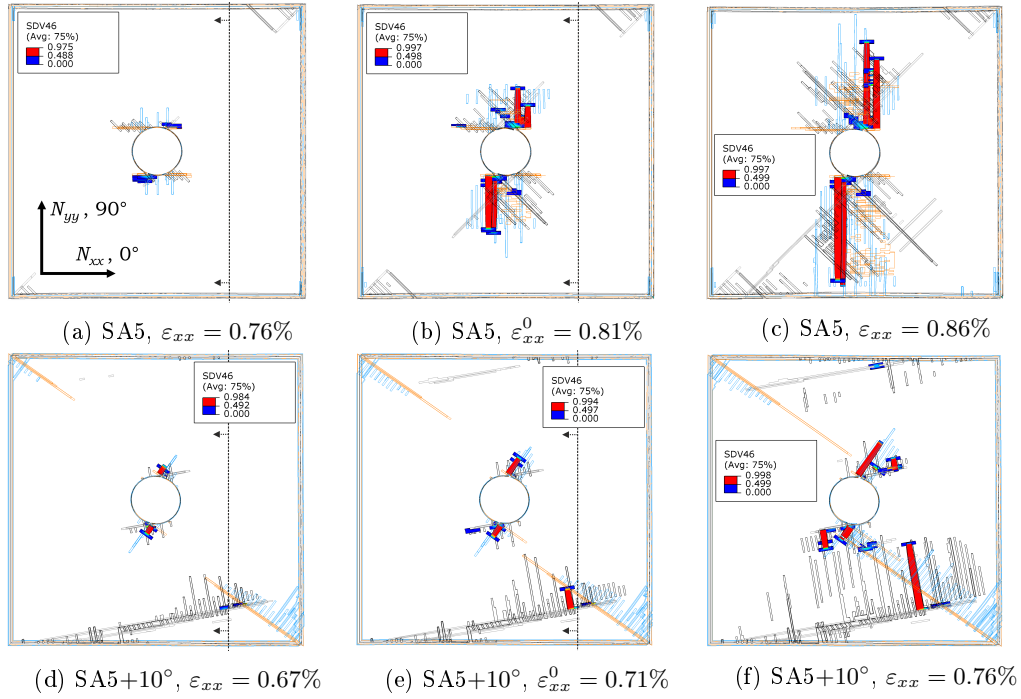
Figure 14: Propagation of fibre damage $d_F > 0$ (SDV46 - represented in a colour map from blue to red) along with intralaminar matrix cracking in SA5, unmodified and after rotation, at three strain states (before, at and after ultimate failure) from FEA. Rotation leads to a change in failure type: from hole-driven to edge driven failure. ε_{xx} corresponds to applied strain and ε_{xx}^0 corresponds to applied strain at ultimate failure. Matrix cracks are shown in black, orange, grey and cyan from lowest to highest ply angle; this order corresponds to $-45°$, $0°$, $+45°$, $90°$ in unrotated state, and to $-80°$, $-35°$, $+10°$, $+55°$ after rotation, respectively. Transparency added to the material to make matrix cracks and fibre damage visible in every ply. Loading direction in x. Cross-section locations are highlighted with dotted lines. These are taken at 9 mm away from the centre of the hole in the x direction.

(a) SA5, $\varepsilon_{xx} = 0.76\%$ (b) SA5, $\varepsilon_{xx}^0 = 0.81\%$

(c) SA5+10°, $\varepsilon_{xx} = 0.67\%$ (d) SA5+10°, $\varepsilon_{xx}^0 = 0.71\%$
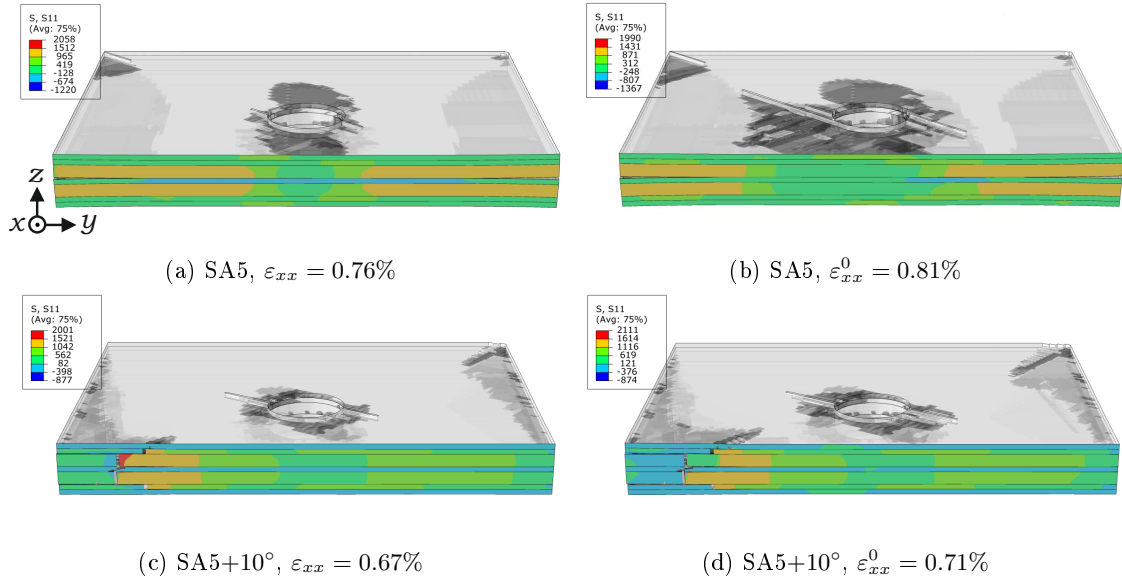
Figure 15: Cross-sections of SA5, unmodified and after rotation, at two strain states (before and at ultimate failure) taken at 9 mm away from the centre of the hole in the x direction from FEA. Figures (a), (b), (c) and (d) correspond to cross-sections in Figure 14a, 14b, 14d and 14e, respectively. Fibre stresses σ_{11} (in MPa) are shown in a colour map from blue to red on the cross-section plane. Delaminations and matrix cracks are displayed in translucent greyscale. Figure illustrates differences in concentration and unloading of σ_{11} for hole-driven and edge-driven failure.

26

Figure 16: FE predicted stress-strain curves of SA and NSA laminates, with (+10°) and without rotation, with (+E) and without edge treatment, for different ply blocking strategies.

Table 1: IDs and corresponding stacking sequences of laminates simulated with FEA. Number of experimentally tested cases also indicated.

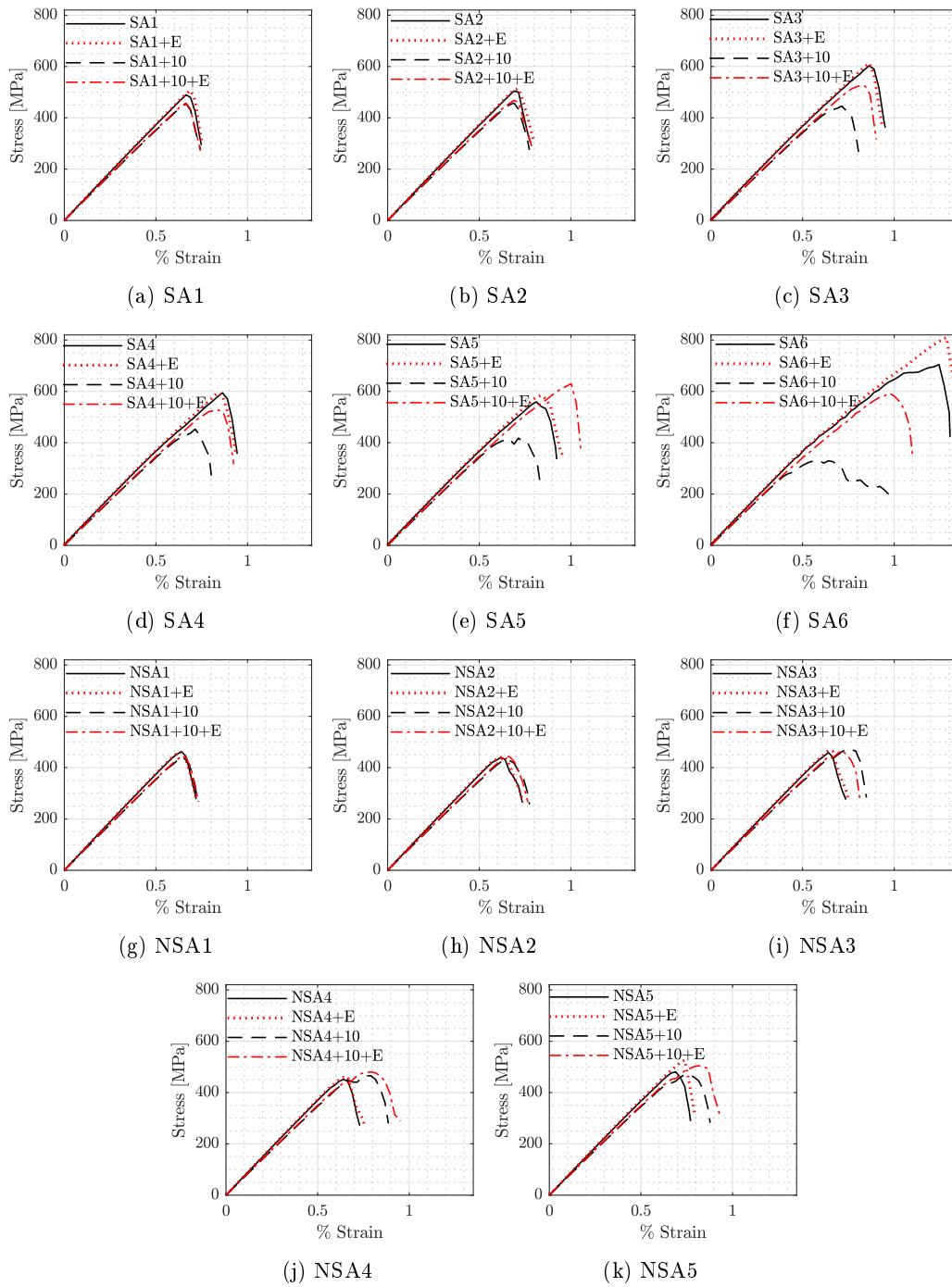| ID	Stacking sequence	Exp.
SA1	$[45/0/\text{-}45/0/\text{-}45/0/45/0/90/0_2/90/0/\text{-}45/0/45/0/45/0/\text{-}45]$	3
SA2	$[45/\text{-}45/0_2/\text{-}45/45/0_2/90/0_2/90/0_2/\text{-}45/45/0_2/45/\text{-}45]$	3
SA3	$[45/\text{-}45/45/\text{-}45/0_4/90/0]_\text{S}$	3
SA4	$[45/\text{-}45/45/\text{-}45/0_5/90]_\text{S}$	-
SA5	$[45_2/\text{-}45_2/0_5/90]_\text{S}$	-
SA6	$[45_2/\text{-}45_2/90/0_5]_\text{S}$	-
NSA1	$[10/\text{-}10/\text{-}57/57/\text{-}10/10/57/\text{-}57/10/\text{-}10_2/10/57/\text{-}57/\text{-}10/10/\text{-}57/57/10/\text{-}10]$	3
NSA2	$[57/\text{-}57/57/\text{-}57/10/\text{-}10/10/\text{-}10/10/\text{-}10]_\text{S}$	3
NSA3	$[\text{-}57_2/57_2/10_2/\text{-}10_3/10]_\text{S}$	3
NSA4	$[\text{-}57_2/57_2/10/\text{-}10_3/10_2]_\text{S}$	-
NSA5	$[\text{-}57_2/57_2/10_3/\text{-}10_3]_\text{S}$	-
SA3+5°	$[50/\text{-}40/50/\text{-}40/5_4/\text{-}85/5]_\text{S}$	3
NSA2+5°	$[62/\text{-}52/62/\text{-}52/15/\text{-}5/15/\text{-}5/15/\text{-}5]_\text{S}$	3
SA1+10°	$[55/10/\text{-}35/10/\text{-}35/10/55/10/\text{-}80/10_2/\text{-}80/10/\text{-}35/10/55/10/55/10/\text{-}35]$	1
SA2+10°	$[55/\text{-}35/10_2/\text{-}35/55/10_2/\text{-}80/10_2/\text{-}80/10_2/\text{-}35/55/10_2/55/\text{-}35]$	1
SA3+10°	$[55/\text{-}35/55/\text{-}35/10_4/\text{-}80/10]_\text{S}$	3
SA4+10°	$[55/\text{-}35/55/\text{-}35/10_5/\text{-}80]_\text{S}$	-
SA5+10°	$[55_2/\text{-}35_2/10_5/\text{-}80]_\text{S}$	-
SA6+10°	$[55_2/\text{-}35_2/\text{-}80/10_5]_\text{S}$	-
NSA1+10°	$[20/0/\text{-}47/67/0/20/67/\text{-}47/20/0_2/20/67/\text{-}47/0/20/\text{-}47/67/20/0]$	-
NSA2+10°	$[67/\text{-}57/67/\text{-}57/20/0/20/0/20/0]_\text{S}$	3
NSA3+10°	$[\text{-}47_2/67_2/20_2/0_3/20]_\text{S}$	-
NSA4+10°	$[\text{-}47_2/67_2/20/0_3/20_2]_\text{S}$	-
NSA5+10°	$[\text{-}47_2/67_2/20_3/0_3]_\text{S}$	-
SO	$[45/\text{-}45/0/45/\text{-}45/90/45/\text{-}45/45/\text{-}45]_\text{S}$	[22]
QI	$[\text{-}45/0/45/90]_{2\text{S}}$	[22]
HA	$[0/45/0/90/0/\text{-}45/0/45/0/\text{-}45]_\text{S}$	[22]

Table 2: Ply properties of AS4/8552 unidirectional prepreg. All properties from [22] except for f_T, f_C and f_G, which were assumed from IM7/8552 material system [28]. Ply thickness of 0.195 mm was measured from experiments.

Ply properties			
Elastic		**Fracture**	
E_{11}^+, E_{11}^- (GPa)	137.1, 114.3	$\mathcal{G}_1^+$ (kJ/m^2)	125.0
E_{22}^+, E_{22}^- (GPa)	8.8, 10.1	$\mathcal{G}_1^-$ (kJ/m^2)	61.0
G_{12}, G_{13} (GPa)	4.9	$\mathcal{G}_2^+$ (kJ/m^2)	0.30
ν_{12}, ν_{13}	0.314	$\mathcal{G}_6$ (kJ/m^2)	0.87
ν_{23}	0.487	f_G	0.3
Strength		**Thermal**	
X_T (MPa)	2106.4	α_1 (°C^{-1})	$0.21 \cdot 10^{-6}$
X_C (MPa)	-1675.9	α_2 (°C^{-1})	$3.30 \cdot 10^{-5}$
Y_T (MPa)	74.2		
Y_C (MPa)	-322.0		
S_L (MPa)	110.4		
f_T	0.4		
f_C	0.2		